



# Photocatalytic benzylamine coupling dominated by modulation of linkers in donor-acceptor covalent organic frameworks

Jinfang Kou<sup>1</sup>, Ganping Wang<sup>1</sup>, Hongyan Guo, Liang Li, Jian Fang, Jiantai Ma, Zhengping Dong\*

State Key Laboratory of Applied Organic Chemistry, Laboratory of Special Function Materials and Structure Design of the Ministry of Education, College of Chemistry and Chemical Engineering, Lanzhou University, Lanzhou 730000, PR China

## ARTICLE INFO

### Keywords:

Covalent organic frameworks  
Photocatalysis  
Donor-acceptor  
Excitonic effects  
Benzylamine coupling

## ABSTRACT

The strong excitonic effect is widely prevalent in covalent organic frameworks (COFs)-based catalysts, while the high exciton binding energies ( $E_b$ ) of COFs seriously limit their photocatalytic performance. Herein, theoretical calculations are conducted to evaluate the  $E_b$  values of potential COFs derived from benzo[1,2-b:3,4-b']trithiophene-2,5,8-tricarbaldehyde (BTT) and 2,4,6-trihydroxybenzene-1,3,5-tricarbaldehyde (Bp) as aldehyde monomers. Diverse aromatic amine linkers including dipyridine diamine (BPy), biphenyl diamine (BPh), and *p*-phenylenediamine (MPH) with different molecular lengths and N-sites are used as linker models to regulate the excitonic effect. The obtained BTT-BPy-COF with a long BPy linker and the lowest calculated  $E_b$  value possesses the best photocatalytic performance for benzylamine coupling, with conversion and selectivity up to 99% accompanied by a high oxidation rate, outperforming most of the reported works. Further mechanistic investigation reveals that the bipyridine-N sites in BTT-BPy-COF exhibit strong electron transfer as well as enhanced  $O_2$  adsorption and activation that is beneficial to photocatalytic benzylamine coupling.

## 1. Introduction

Visible-light-driven photoredox reactions can be used to convert solar energy into chemical energy via the formation of chemical fuels. These reactions, including carbon dioxide ( $CO_2$ ) reduction [1,2], organic reactions [3,4], and water splitting [5–7] are considered to be an effective solution for meeting environmental challenges and addressing the unsustainable energy crisis. Since the first report of  $TiO_2$  as a photocatalyst [8], various inorganic semiconductor photocatalysts such as metal oxides, nitrides, sulfides, and phosphides have been developed [9,10]. Recently, organic semiconductor photocatalysts have emerged as promising photocatalysts due to their low toxicity and cost-effectiveness [11–13]. Poly(*p*-phenylene) was the first reported organic semiconductor when its use as a hydrogen evolution photocatalyst was described in 1985. However, the poor performance and narrow UV-Vis spectrum of poly(*p*-phenylene) have limited its further application [14]. After that, various organic materials with high activity for photocatalysis were reported, including materials based on carbon nitrides [15],  $\pi$ -conjugated polymers [16,17], and covalent triazine-based

frameworks (CTFs) [18]. However, these organic materials often do not have well-organized structures, which constrains the transfer of photoinduced electrons and limits photocatalytic activity [19,20]. The separation of photoinduced electrons via the adjoin effect in the majority of polymer semiconductors with strong light absorption properties is a well-accepted photocatalytic mechanism. However, this well-known concept ignores strong excitonic effects (the Coulomb interactions between photoinduced electrons and holes in the bound state) [21], which are significant for photocatalysts. The exciton binding energy ( $E_b$ ) is a crucial factor for assessing the excitonic effect of photocatalysts and illustrating the strength of the Coulomb interaction. However, the design and fabrication of organic semiconductors featuring reduced  $E_b$  values is a persistent challenge that must be overcome to develop effective photocatalysts.

Various approaches have been devised to reduce the  $E_b$  value of organic semiconductor materials, including the use of donor-acceptor (D-A) molecular junctions [22], homojunctions [23], and heterojunctions [22]. These strategies promote the separation of excitons and boost the photocatalytic performance. A photocatalyst containing a D-A

\* Corresponding author.

E-mail address: [dongzhp@lzu.edu.cn](mailto:dongzhp@lzu.edu.cn) (Z. Dong).

<sup>1</sup> These authors contributed equally to this work.

junction can be stimulated by light, prompting electrons to migrate from the donor to the electrophilic acceptor. This accelerates the charge transfer, which, hinders the recombination of charge carriers. Unfortunately, constructing D-A junctions in organic semiconductor materials is very challenging due to the disordered structures of polymers. Recent studies have shown that covalent organic frameworks (COFs) are organic semiconductors with high crystallinity and modular synthetic versatility. Moreover, the  $E_b$  value of COFs can sometimes be controlled by regulating the monomers, offering a potential strategy for developing high-performance photocatalysts [24–27]. Employing monomers to build an ordered stacking structure allows COFs to possess a high degree of structural tenability, while different linker lengths and  $E_b$  values provide remarkable differences in photocatalytic performance [13,28,29]. Accordingly, the design and fabrication of optimal COFs with low  $E_b$  values is a highly promising strategy. Jiang et al. regulated excitonic effects in a COF by photocatalytic molecular oxygen [30]. Zhang et al. employed computational methods to accommodate the excitonic effects in a COF, achieving enhanced photocatalytic activity [31]. Xie et al. outlined the relationship between excitonic behavior and photocatalytic performance [13]. Nevertheless, formulating practical strategies for achieving the lowest possible  $E_b$  in various donor-acceptor (D-A) structures to optimize COF-based photocatalysts remains an ongoing challenge.

The diversity of possible building blocks endows well-designed COFs with particular topologies, verified pore sizes, tailored functions, and controllable  $E_b$  values. Regulating the linkers and selecting COF building units with heteroatom-based functionality to accurately control the  $E_b$  of COFs is a potentially feasible strategy for screening optimal photocatalysts. However, this strategy has been rarely reported. Lang et al. recently investigated the influence of linker length on photocatalytic activity, reporting that a longer linker length led to lower performance due to slightly inferior optoelectronic properties [32]. Moreover, some pioneer works have demonstrated that  $g\text{-C}_3\text{N}_4$ , CTFs, and poly-triazine imides (PTIs) [33–35], which are all N-containing organic reaction photocatalysts, show different photocatalytic performance due to their different N-containing functional groups. Heteroatom species such as nitrogen may also affect the excitonic effect of COF-based photocatalysts, so this phenomenon deserves additional research attention.

In this work, to provide a clear viewpoint for regulating the photocatalytic performance of COF materials, two aldehyde-based monomers and three amine-based monomers were employed to design relevant D-A COFs by DFT simulation, and the designed COFs were experimentally prepared and evaluated. The calculated  $E_b$  values of these COFs follow an increasing trend: BTT-BPy-COF < Bp-BPy-COF; BTT-MPh-COF < Bp-MPh-COF; BTT-BPh-COF < Bp-BPh-COF. The photocatalytic performance of the obtained catalysts was closely related to their  $E_b$  values. It is also worth noting that the pyridine-N of the dipyridine diamine (BPy) in the COFs has a substantial effect on photocatalytic performance due to the induced electronic and spatial variations [36,37]. Hence, the reasonable design of nitrogen-containing heterocycles in COFs and modulate the linkers are effective strategies for regulating the activity of COF-based photocatalysts. The experimental results show that the photocatalytic performance of the prepared six COFs aligns well with DFT calculations. BTT-BPy-COF possesses the highest photocatalytic performance in addition to excellent stability and recyclability for the benzylamine coupling reaction.

## 2. Experimental section

### 2.1. Materials

Benzo[1,2-b:3,4-b'-b'']trithiophene-2,5,8-tricarbaldehyde (BTT) and 1,3,5-triformylphloroglucinol (Bp) were purchased from Shanghai Macklin Biochemical Technology Co., Ltd. Biphenyl diamine (BPh), BPy and p-phenylenediamine (MPh) were purchased from Tianjin Heowns Biochemical Reagent Co., Ltd. Ortho-dichlorobenzene (o-DCB) and N, N-

dimethylformamide (DMF) were provided by Lianlong Bohua (Tianjin) Pharmaceutical Chemistry Co., Ltd. All the commercially available reagents were used as received without further purification.

### 2.2. Synthesis procedure of BTT-BPh-COF, BTT-BPy-COF and BTT-MPh-COF

Typically, a Pyrex tube was charged with BTT (0.2 mmol, 66.0 mg) and BPh (0.3 mmol, 54.7 mg). o-DCB (1.5 mL) and n-butyl alcohol (n-BuOH, 1.5 mL) were introduced into the above tube and the mixture was uniformed through sonication for a duration of 10 minutes. Then, 6 M aqueous acetic acids (0.5 mL) were added to serve as a catalyst. The pyrex tube was rapidly frozen using liquid nitrogen (77 K), purged with air and sealed by flame. The reaction mixture was subsequently heated at 120 °C for a duration of 3 days. After cooling to ambient temperature, the obtained yellow-orange powder was filtrated and rinsed with THF, CH<sub>3</sub>OH and C<sub>2</sub>H<sub>5</sub>OH for more than three times. The support materials were dried at 80 °C under vacuum for 12 h. BTT-BPy-COF and BTT-MPh-COF were prepared according to the same procedure of BTT-BPh-COF; using BTT and BPy as precursors for BTT-BPy-COF, BTT and MPh as precursors for BTT-MPh-COF.

### 2.3. Synthesis procedure of Bp-BPh-COF, Bp-BPy-COF and Bp-MPh-COF

Bp (0.3 mmol, 63 mg) and corresponding amines MPh (0.45 mmol, 48 mg) or BPh (0.45 mmol, 82 mg) were charged in a Pyrex tube. Dioxane (1.5 mL) and mesitylene (1.5 mL) were introduced into the above solution and the mixture were uniformed in ultrasonication at room temperature, then the 6 M aqueous acetic acid (0.5 mL) were added. The mixture was frozen in an N<sub>2</sub> liquid bath (77 K) and then sealed under vacuum after three freeze-pump-thaw cycles. The solution was transferred into an oven and stayed at 120 °C for 72 h. After cooling to room temperature, the precipitate was filtered separation and washed with acetone and tetrahydrofuran for more than three times. The precipitate was dried to obtain the corresponding COFs under vacuum at 80 °C. The synthesis of Bp-BPy-COF was similar to Bp-MPh-COF except dioxane (1.5 mL) and mesitylene (1.5 mL) was replaced by o-DCB (0.75 mL) and N, N-dimethylacetamide (2.25 mL).

### 2.4. General procedure for photocatalytic oxidation of benzylamine to imine

Benzylamine (0.5 mmol), photocatalyst (10 mg), CH<sub>3</sub>CN (3 mL) were added into a tube with a magneton. The above mixture was stirred for 3 hours with an oxygen balloon under the blue LED light irradiation. After the reaction was finished, the catalyst was isolated through centrifugation and washed with C<sub>2</sub>H<sub>5</sub>OH for more than 6 times. The obtained organic phases were evaporated under vacuum to give the crude product.

### 2.5. Electrochemical measurements

Electrochemical measurements were proceeded in a three-electrode cell with an electrochemical station. 6 mg COF powder were ultrasonically dispersed in 1 mL H<sub>2</sub>O/C<sub>2</sub>H<sub>5</sub>OH mixture to form a highly-dispersed slurry (ink). The resulted slurry was dripped into indium tin oxide (ITO) coated glasses and dried by infrared irradiation. Meanwhile, the 0.1 M Na<sub>2</sub>SO<sub>4</sub> water solution was acted as electrolyte. A platinum wire, an Ag/AgCl electrode and a coated ITO conductive glass were supplied as counter electrode, reference electrode and working electrode, respectively. The 465 nm blue LEDs were placed at 3 cm away from the electrochemical cell to serve as a source light.

### 2.6. Characterizations

The crystal structure of photocatalysts were recorded by powder X-

ray diffraction patterns (PXRD) on Rigaku MiniFlex 600 diffractometer with Cu-K $\alpha$  radiation. The nitrogen physisorption isotherms were measured at 77 K using ASAP 2460 instrument. The specific surface area of photocatalysts were obtained by Brunauer-Emmett-Teller (BET) method, the pore size and pore volume were calculated from the sorption curve by using the nonlocal density functional theory (NLDFT) model. The Fourier transform infrared (FT-IR) spectra of solid samples were recorded on Bruker spectrometer (VERTEX 70) ranging from 4000 to 400 cm<sup>-1</sup>. Scanning electron microscopy (SEM) were performed on Thermo Fisher Apreo S field emission electron microscope. Transmission electron microscopy (TEM) characterizations were performed on FEI talos F200s. Thermogravimetric (TGA) were conducted on TA-Q50 thermogravimeter analyzer under nitrogen atmosphere from 30 °C to 800 °C at the rate of 10 °C/min. X-ray Photoelectron Spectroscopy (XPS) was used to examine the elemental composition and bonding states of the catalysts using a PerkinElmer PHI-5702. The Solid-state <sup>13</sup>C cross polarization magic angle spinning (<sup>13</sup>C CP-MAS) NMR spectroscopy was recorded on AVANCE NEO 600 MHz WB FT NMR. The light absorption capacity of all photoelectrodes were determined by UV-Vis absorption spectra (UV-Vis) (Hitachi U-4000) with BaSO<sub>4</sub> as the reference. The conversion and selectivity of the photocatalytic reaction were measured by gas chromatography (GC) equipped with a flame ionization detector (GC-FID, Agilent 8890). Gas chromatography-mass spectrometry (GC-MS) were performed on Agilent 5977E. The conversion and selectivity for benzylamine coupling were determined as follows:

$$\text{Conversion (\%)} = [(C_0 - C_r)/C_0] \times 100\%$$

$$\text{Selectivity (\%)} = [C_p/(C_0 - C_r)] \times 100\%$$

C<sub>0</sub> represents the initial concentrations of the reactant; C<sub>r</sub> is the concentration of substrate and C<sub>p</sub> shows the concentration of the product.

## 2.7. DFT calculations

D-A pair for structure optimization, energy, electronic properties, and wave function were calculated using Gaussian 09 package and calculation level is pbe38/6-311 g(d,p) [38]. The polarizable continuum model (PCM) was used to consider the effect of acetonitrile solvation [39]. Multiwfn was used for electron-hole analysis to analyze optical properties [40,41]. For the simulation of periodic COF structure the VASP (Vienna Ab-initio Simulation Package) calculations were used, the Perdew-Burke-Ernzerh of exchange-correlation functional was used for the structure optimization, and the hse06 hybrid functional was used for the calculation of the electronic structure [42–44]. In the above

calculations, the truncation energy was set to 450 eV, the convergence criterion for the electron step was 10E-6 eV, and the convergence criterion of forces during atomic optimizations was 0.03 eV/Å. The Brillouin zone was sampled using a 3\*3\*1  $\Gamma$ -centered K point. Interactions between the layers of COFs were eliminated using a vacuum region of about 15 Å.

## 3. Results and discussion

The imine bond (C=N), as one of the most universally employed linkages, is usually utilized to build COF materials [45–47]. Herein, two classical photosensitizers, benzo[1,2-b:3,4-b'-b'']trithiophene-2,5,8-tricarbaldehyde (BTT) and 2,4,6-trihydroxybenzene-1,3,5-tricarbaldehyde (Bp), were selected as aldehyde monomers (Scheme 1). Schiff-base condensation was employed to link BTT or Bp with one of three aromatic amine linkers: BPy, BPh, and MPh. Thus, six imine-bridged COFs were formed. These COFs were denoted as BTT-BPy-COF, BTT-BPh-COF, BTT-MPh-COF, Bp-BPy-COF, Bp-BPh-COF, and Bp-MPh-COF. To screen these amine-aldehyde pairs for useful D-A pairs and to predict the photocatalytic activity of the different COFs, the highest occupied

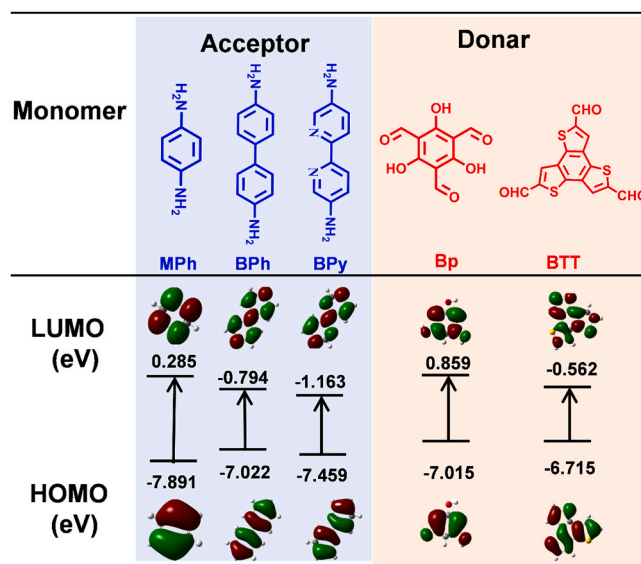
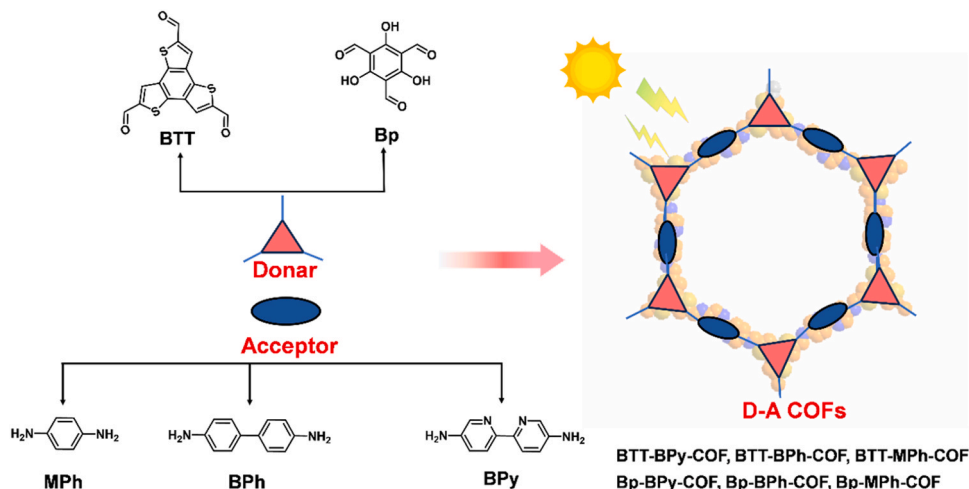


Fig. 1. HOMO and LUMO energy level diagram for the two types of building blocks for constructing D-A pairs.



Scheme 1. The synthesis procedure of D-A COFs composed by amine monomers and aldehyde monomers for photocatalytic reaction.

molecular orbital (HOMO) and the lowest unoccupied molecular orbital (LUMO) energy levels of all the monomers were first calculated via DFT (Fig. 1).

Previous studies have demonstrated that a D-A structure is formed when the HOMO and LUMO of the monomers are staggered, with the acceptor and donor primarily contributing to the LUMO and HOMO, respectively [31,48]. As shown in Fig. 1, BTT can form frontier orbitals staggered with BPh, MPh, and especially BPy. The exciton effect is an important factor affecting the photocatalytic performance of COFs, and the  $E_b$  value is commonly used to measure the exciton effect of semiconductors. A lower  $E_b$  value indicates a longer exciton lifetime and a more favorable photocatalytic reaction. The  $E_b$  values of D-A pairs can be used to qualitatively analyze the charge separation ability of the corresponding D-A COFs after photoexcitation [49]. The  $E_b$  energies of the six D-A pairs were calculated using multiwfn with the following formula [40,49,50]:

$$E(b) = \iint \frac{\rho^{\text{hole}}(r_1)\rho^{\text{ele}}(r_2)}{|r_1 - r_2|} dr_1 dr_2$$

The  $E_b$  energies of the six D-A pairs from low to high are 3.71 eV (BTT-BPy), 4.23 eV (BTT-MPh), 4.37 eV (BTT-BPh), 4.50 eV (Bp-BPh), 4.53 eV (Bp-BPy), and 5.23 eV (Bp-MPh) (Figure S1). Notably, the  $E_b$  values of the D-A pairs with BTT as the electron donor are lower than those with Bp as the electron donor. Thus, from the point of view of the exciton effect, it can be inferred that the COFs designed with BTT as the electron donor have better photocatalytic performance than those designed with Bp as the electron donor. This implies that, via modulating the linkers and the modules, the optimal BTT-BPy-COF with the lowest  $E_b$  value should exhibit superior photocatalytic activity.

Based on the obtained theoretical calculation results, three typical COFs (BTT-BPy-COF, BTT-BPh-COF, and BTT-MPh-COF) were experimentally prepared in a mixture of *n*-BuOH and *o*-DCB. Acetic acid was used as the catalyst, and the reaction was performed at 120 °C for 3 days (Fig. 2). The BTT-COFs remained undissolved in common solvents and were washed with DMF, CH<sub>3</sub>OH, and C<sub>2</sub>H<sub>5</sub>OH to afford yellow-orange powders. The chemical structures of the BTT-COFs and their monomers were investigated by FT-IR spectroscopy (Fig. 3a, Figs. S2–4) and <sup>13</sup>C CP-MAS NMR spectroscopy (Fig. 3b). As shown in Figs. S2–4, the FT-IR spectra of all the synthesized COFs show the presence of the characteristic phenyl group. A stretching vibration at 3030 cm<sup>−1</sup> and a skeleton vibration at 1625–1450 cm<sup>−1</sup> indicate well-defined skeleton frameworks [51]. In addition, the formation of C=N linkages is verified by the characteristic peak at about 1599 cm<sup>−1</sup> [52]. The -CHO peak at

1662 cm<sup>−1</sup> and -NH<sub>2</sub> stretching band at about 3300 cm<sup>−1</sup> are significantly attenuated compared with the aldehyde group of BTT and amino groups of BPy, BPh and MPh, demonstrating that the BTT-COFs have a high degree of polymerization due to Schiff-base condensation [53,54]. The solid-state <sup>13</sup>C NMR spectra of the BTT-COFs show a clear peak at 152.8 ppm attributed to the carbon atom of the imine bond [55]. This indicates the successful covalent condensation of BTT with the BPy, BPh, and MPh organic amines to form BTT-BPy-COF, BTT-BPh-COF, and BTT-MPh-COF. The peak at 153 ppm is ascribed to the ortho-carbon of nitrogen on the pyridine ring. Many strong peaks can be observed in the range of 120–160 ppm. These peaks are attributed to the carbon in phenyl units, alkyl groups, and thiazole groups in the COF frameworks, in accordance well with their structures. These results confirm the successful preparation of the three BTT-COFs.

The intrinsic porosity of the BTT-COFs was assessed by nitrogen adsorption-desorption isotherms obtained at 77 K (Fig. 3c). These isotherms show a sharp uptake of nitrogen gas below a relative pressure of  $p/p_0=0.01$  and a step in the region of  $p/p_0=0.01-0.4$ . Thus, the isotherms can be classified as type IV. The calculated Brunauer-Emmett-Teller (BET) surface areas of BTT-BPy-COF, BTT-BPh-COF, and BTT-MPh-COF are 729.31, 1435.32, and 884.96 m<sup>2</sup>g<sup>−1</sup>, respectively (Table S1). Although the surface areas of photocatalysts are a vital aspect of their surface morphology, photocatalytic performance for benzylamine coupling is not directly proportional to the BET specific surface area because the large benzylamine substrate means that pores smaller than 0.5 nm may not be involved in the reaction [56]. The pore size distributions (PSDs) of the prepared COFs were calculated using the nonlocal density functional theory (NL-DFT) equilibrium model. The PSDs of BTT-BPh-COF and BTT-MPh-COF indicate that both materials possess a microporous-mesoporous structure, which is confirmed by their rapid nitrogen uptakes at a very low relative pressure. In contrast, BTT-BPy-COF displays a microporous distribution centered at 1.9 nm, which is in agreement with the predicted and simulated Gaussian structural model (Figure S5) [57].

The morphologies of the BTT-COFs were characterized via SEM and TEM (Fig. 4a–g, Figs. S6–7, S9–10). BTT-BPy-COF shows a rod-like network morphology composed of two-dimensional nanorods, while BTT-BPh-COF and BTT-MPh-COF show honeycomb and columnar morphologies (Figures S6 and S9). The structural characteristics of the BTT-COFs were then visualized by TEM and HRTEM. Selected area electron diffraction (SAED) confirms the highly ordered structure of BTT-BPy-COF (Fig. 4c). The elemental distribution and composition were investigated by EDS mapping. The prepared BTT-COFs show a

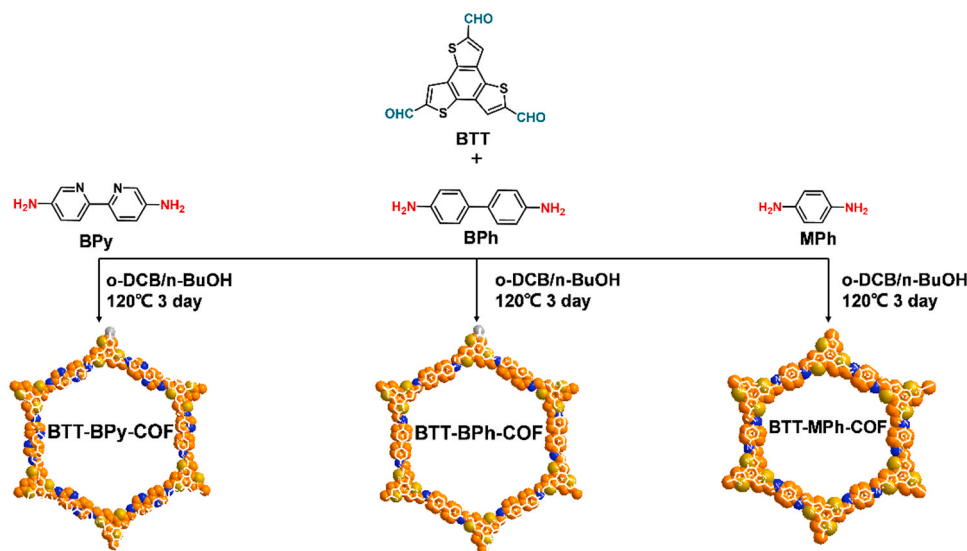
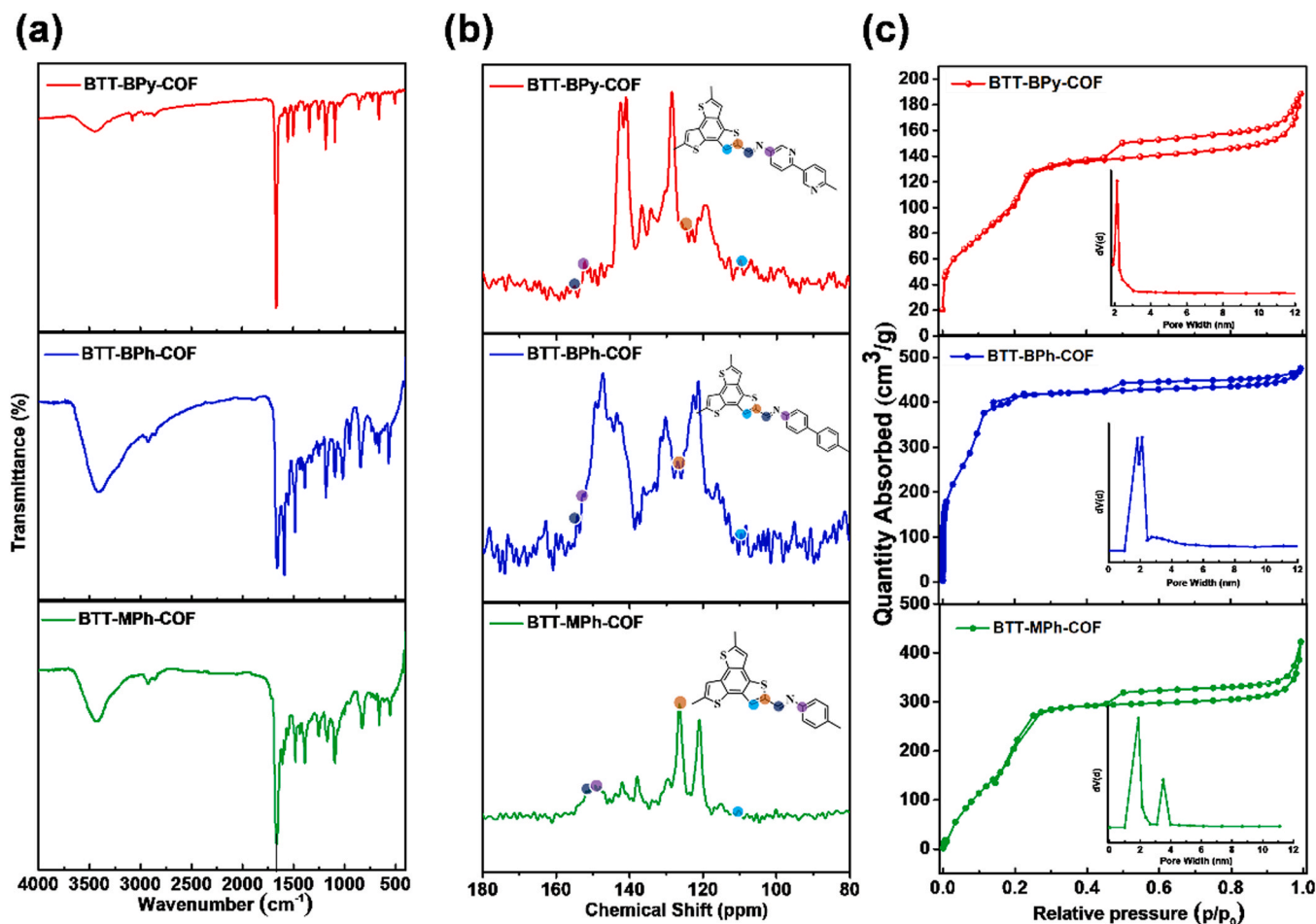


Fig. 2. The reaction condition and chemical structure of BTT-BPy-COF, BTT-BPh-COF and BTT-MPh-COF.





**Fig. 3.** (a) The FT-IR of BTT-BPy-COF, BTT-BPh-COF and BTT-MPh-COF. (b) The solid state <sup>13</sup>C NMR of BTT-BPy-COF, BTT-BPh-COF and BTT-MPh-COF. (c) The BET curves of BTT-BPy-COF, BTT-BPh-COF and BTT-MPh-COF.

uniform and homogeneous distribution of C, N, and S (Fig. 4d–g, Figures S8, S11). XPS further demonstrates the existence of C, N, and S elements in the prepared BTT-COFs (Figures S12–14). The high-resolution C 1s spectra of the BTT-COFs were deconvoluted into three peaks ascribed to C=C–N, C=C/C–C, and C=C–S. Elemental analysis shows that the C, H, N, and S content of the BTT-COFs are in agreement with the theoretical calculations (Table S2). A stable COF structure is desirable for practical catalytic applications. Therefore, TGA was performed under a nitrogen atmosphere (Figure S15). The prepared BTT-COFs do not exhibit significant mass loss up to 300 °C. PXRD was performed (Fig. 5a–c) and theoretical structure simulations were evaluated using the Materials Studio package to elucidate the crystal structures of the BTT-COFs. All the BTT-COFs possess hexagonal 2D nets with hcb topology [58]. The PXRD patterns of the BTT-COFs and their monomers were also compared (Figures S16–18), demonstrating the purity of the BTT-COFs. The sharp reflections in the low-angle region demonstrate the highly crystalline and long-range ordered structure of the synthesized BTT-COFs. The diffraction patterns of BTT-BPy-COF, BTT-BPh-COF, and BTT-MPh-COF show an intense (100) peak at  $2\theta=2.77^\circ$ ,  $2.73^\circ$ , and  $3.46^\circ$ , respectively. Peaks corresponding to the (110) and (200) crystal facets can be observed at  $2\theta=4.75^\circ$  and  $5.48^\circ$  for BTT-BPh-COF and  $2\theta=5.99^\circ$  and  $6.93^\circ$  for BTT-MPh-COF. In the BTT-BPy-COF diffraction pattern, peaks at  $2\theta=4.74^\circ$ ,  $5.49^\circ$ ,  $7.25^\circ$ , and  $24.70^\circ$  correspond to the (110), (200), (210), and (001) facets, respectively. The broad peak around  $25^\circ$  might be attributed to the partially amorphous phase in the BTT-COFs. The simulated PXRD profiles of the AA-type stacking model are also consistent with the experimental patterns. This illustrates that the as-prepared BTT-COFs have an eclipsed

arrangement in the P-6 space group and high crystallinity [58]. The unit cells parameters of the prepared COFs are  $a=b=37.189 \text{ \AA}$  and  $c=3.600 \text{ \AA}$  for BTT-BPh-COF,  $a=b=37.189 \text{ \AA}$  and  $c=3.600 \text{ \AA}$  for BTT-BPy-COF, and  $a=b=28.582 \text{ \AA}$  and  $c=3.490 \text{ \AA}$  for BTT-MPh-COF.

To investigate the diverse optoelectronic properties of the prepared BTT-COFs, UV-Vis diffuse reflection spectroscopy was adopted to determine their optical band gaps ( $E_g$ ) (Fig. 6a). All three BTT-COFs display wide visible light adsorption ranges due to  $\pi$  electron delocalization [31]. Relative to reference samples, the BTT-BPy-COF shows a distinct red-shift due to its stronger and broader absorption capacity up to 700 nm in the visible region which demonstrates the strong light utilization of BTT-BPy-COF. Based on the obtained Tauc plots (Fig. 6b), the  $E_g$  values of BTT-BPy-COF, BTT-BPh-COF, and BTT-MPh-COF are 2.08, 2.15, and 2.12 eV, respectively. The narrower band gap of BTT-BPy-COF leads to wider visible light absorbance. The transient photocurrent responses of the BTT-COFs were obtained to evaluate their charge separation efficiency (Fig. 6c). BTT-BPy-COF has a more intense response than the other two BTT-COFs, indicating superior photoinduced electron separation and transport efficiency.

The HOMO and LUMO were calculated using Mott-Schottky plots to illustrate the electron conduction properties of the BTT-COFs (Fig. 6d). All three BTT-COFs display positive slopes, indicating a negligible energy gap between the flat band position and the conduction band ( $E_{CB}$ ) potential. The band gaps of BTT-BPy-COF, BTT-BPh-COF, and BTT-MPh-COF are  $-0.70$ ,  $-0.28$ , and  $-0.37 \text{ eV}$ , respectively. Combined with the optical  $E_g$ , the valence band ( $E_{VB}$ ) potentials of BTT-BPy-COF, BTT-BPh-COF, and BTT-MPh-COF are estimated to be 1.38, 1.87, and 1.75 eV, respectively. The band structures and densities of states (DOS) of the

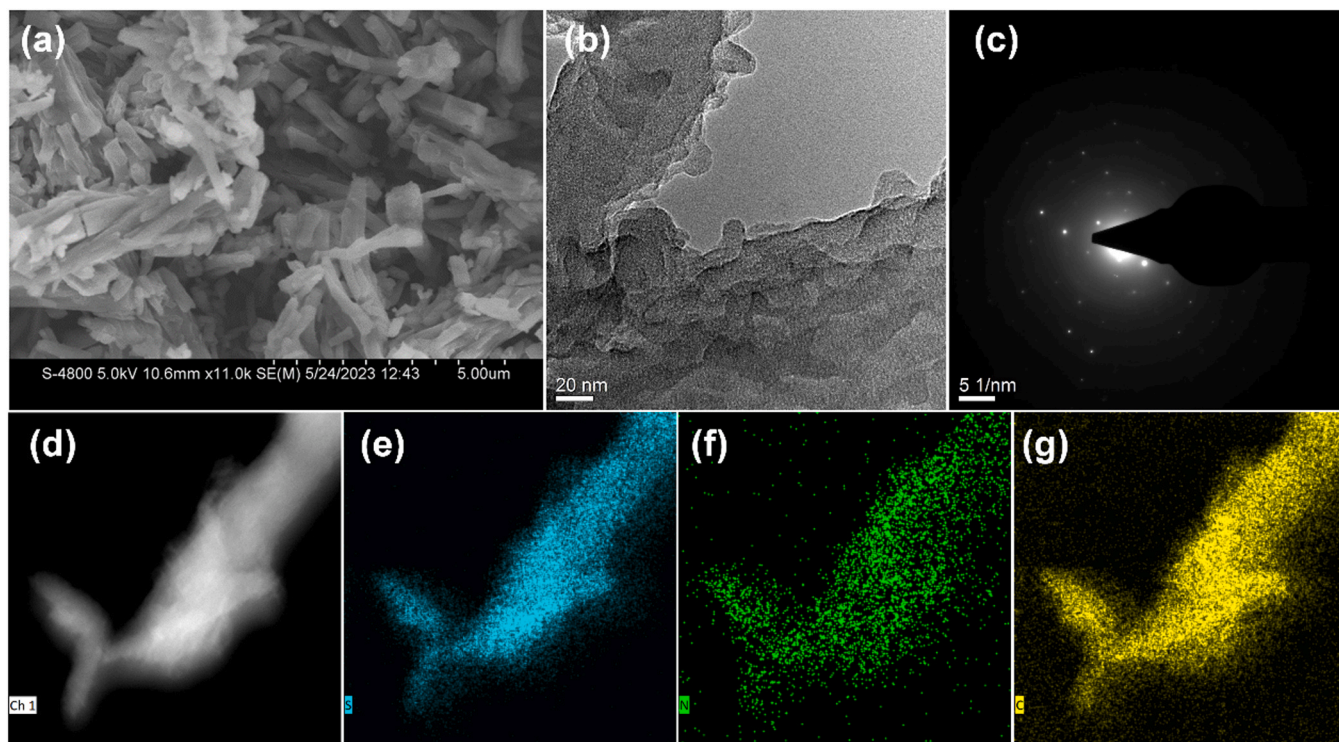


Fig. 4. The (a) SEM and (b)TEM of BTT-BPy-COF and corresponding (c) SAED. (d) The HAADF and (e-g) EDS-mapping of BTT-BPy-COF.

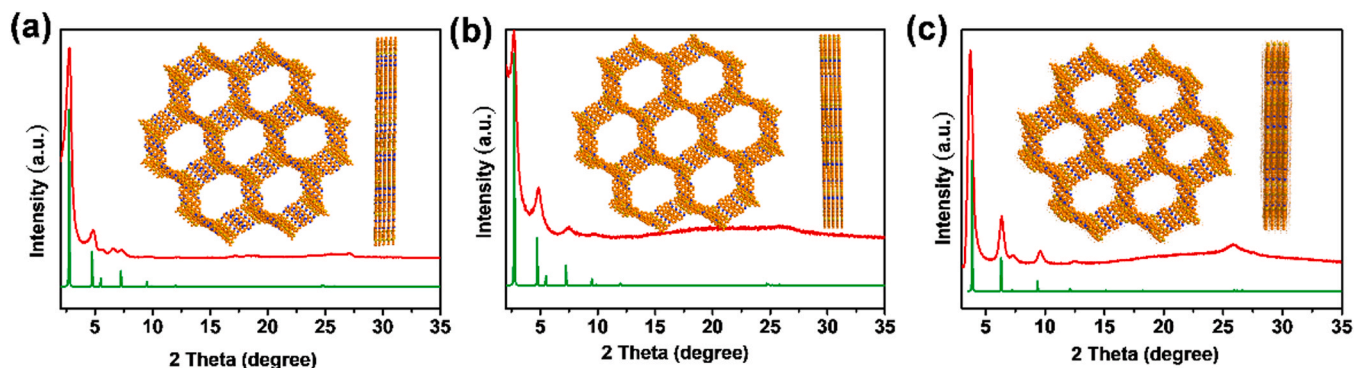


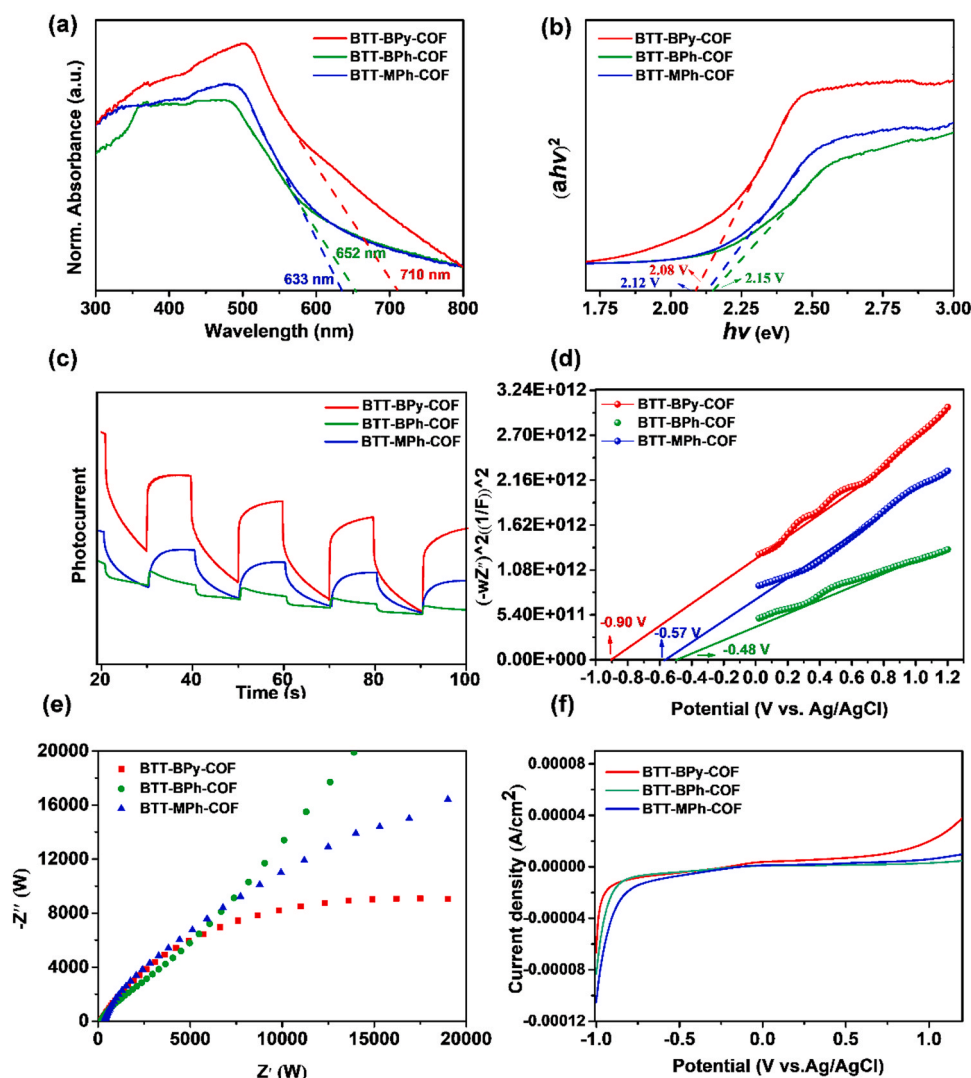
Fig. 5. (a) The experimental PXRD of BTT-BPy-COF (red) and the simulated results of BTT-BPy-COF (green). (b) The experimental PXRD of BTT-BPh-COF (red) and the simulated results of BTT-BPh-COF (green). (c) The experimental PXRD of BTT-MPh-COF (red) and the simulated results of BTT-MPh-COF (green).

COFs were calculated by the HSE06 functional. The calculated band gaps of BTT-BPy-COF, BTT-BPh-COF, and BTT-MPh-COF are 2.34 eV, 2.32 eV, and 2.27 eV, respectively, which are very close to the experimental results (Figures S19–22). The  $E_{VB}$  potential of BTT-BPy-COF indicates that this material shows good potential for amine oxidation but will be less effective for water oxidation and the oxidative generation of  $\cdot OH$  radicals [59].

Photocurrent tests were employed to evaluate the photoinduced excitons and charge carrier separation efficiency of the BTT-COFs. The results imply that BTT-BPy-COF possesses the strongest photocurrent response and most efficient charge transfer of the three BTT-COFs. Electrochemical impedance spectroscopy (EIS) measurements were performed to confirm the reduced interfacial charge transfer resistance of BTT-BPy-COF compared to the other two BTT-COFs (Fig. 6e). EIS was also used to compare the charge separation and electrical conductivity of the prepared photocatalysts. The semicircle radii of the Nyquist plots follow the trend BTT-BPy-COF < BTT-MPh-COF < BTT-BPh-COF, in accordance with the  $E_g$  values. Therefore, BTT-BPy-COF has the lowest charge-transfer resistance ( $R_{ct}$ ). In addition, linear sweep voltammetry

(LSV) curves demonstrate that BTT-BPy-COF possesses the largest current density and the best photoelectrochemical performance compared to the other two photocatalysts (Fig. 6f). Therefore, the above optoelectronic properties investigation confirms that, the strategy of modulation of the COFs linkers can acquire the optimal COF material with excellent photocatalytic performance.

Imines that contain an unsaturated C=N group are vital intermediates for applications in agrochemicals and pharmaceuticals [60]. Therefore, the photocatalytic aerobic oxidation of primary and secondary amines using the prepared BTT-COFs was attempted. Generating superoxide radical anions from molecular oxygen is a green and sustainable strategy [30]. Considering the intriguing photoelectronic properties of the BTT-COFs, the selective oxidative coupling of amines into imines was explored by utilizing benzylamine as a probe reaction. As listed in Table 1, BTT-BPy-COF exhibits the highest catalytic activity, with a high selectivity of 99% (Table 1, entry 1). The conversion of benzylamine vs. time plot over BTT-BPy-COF under the standard conditions is shown in Fig. 7a. As the amount of benzylamine decreases, the amount of coupling products increases, and other intermediates are not



**Fig. 6.** (a) The UV-Vis DRS of BTT-BPy-COF (red), BTT-BPh-COF (green) and BTT-MPh-COF (blue). (b) Tauc plots of BTT-BPy-COF (red), BTT-BPh-COF (green) and BTT-MPh-COF (blue). (c) Transient photocurrents of BTT-BPy-COF (red), BTT-BPh-COF (green) and BTT-MPh-COF (blue). (d) Mott-Schottky plots of BTT-BPy-COF (red), BTT-BPh-COF (green) and BTT-MPh-COF (blue). (e) EIS Nyquist plots of BTT-BPy-COF (red), BTT-BPh-COF (green) and BTT-MPh-COF (blue). (f) LSV curves of BTT-BPy-COF (red), BTT-BPh-COF (green) and BTT-MPh-COF (blue).

detected. A control experiment was carried out, and the results indicate that the blue LED light source, oxidant  $O_2$  source, and BTT-BPy-COF are indispensable for this photocatalytic reaction. In their absence, only trace or low amounts of imine product are detected (Table 1, entries 2–4). A series of reactive oxygen species (ROS) quenching experiments was performed to evaluate the predominant ROS intermediates in the oxidation process. The addition of isopropanol leads to a negligible decline in yield, indicating that hydroxyl radicals ( $\cdot OH$ ) are not involved in this photocatalytic process (Table 1, entry 6). When *L*-histidine (*L*-his) or *p*-benzoquinone (Bq) are added as  $^1O_2$  and  $O_2^{\cdot -}$  scavengers, sharp declines in conversion from 99% to 47.9% and 13.4% are respectively observed (Table 1, entries 5 and 7). Therefore,  $O_2^{\cdot -}$  is a key radical in this reaction. The addition of  $AgNO_3$  alongside  $O_2$  as an acceptor of photo-generated electrons ( $e^-$ ) inhibits the formation of the desired product (Table 1, entry 8). The utilization of KI as a hole scavenger leads to an *N*-benzylbenzaldimine conversion of just 8.7%. Thus, holes also play a significant role in this selective coupling reaction (Table 1, entry 9). Overall, these results illustrate that the predominant ROS is  $O_2^{\cdot -}$ . A comparison of photocatalytic activity is displayed in Table 1, entries 10–14 and Table S3. Bp-Bpy-COF, Bp-BPh-COF and Bp-MPh-COF were prepared for comparison, the relevant materials characterizations were

displayed in Figure S26–S31. There are two crucial factors that influence the catalytic performance. First, the design of bipyridine-*N* is crucial for achieving good catalytic activity. BTT-BPy-COF and Bp-Bpy-COF, which contain bipyridine groups, display low  $E_b$  values. In contrast, BTT-BPh-COF and Bp-BPh-COF, which contain biphenyl units, show higher  $E_b$  values and worse catalytic performance. Second, the overall activity of the prepared catalysts was closely related to the linker length, as indicated by the apparent differences in the photocatalytic performance of BTT-BPy-COF, BTT-BPh-COF, and BTT-MPh-COF. This is confirmed by DFT calculations and the obtained  $E_b$  values. The increase in linker lengths from MPh to BPh is attributed to the extension of  $\pi$ -conjugation [32]. In addition, BTT-BPy-COF exhibits a wider range of visible light absorption and more suitable redox potential compared to the other two BTT-COFs, which might also benefit its photocatalytic performance.

The performance of BTT-BPy-COF was further investigated by testing a series of amines, as shown in Table 2. For aromatic amines with both electron-donating ( $-CH_3$  and  $-OCH_3$ ) (Tables 2, 2a–f) or electron-withdrawing ( $-F$ ,  $-Cl$ , and  $-Br$ ) groups (Tables 2, 2g–m), imine selectivity and conversion are maintained at high levels ( $> 90\%$ ). Amines with electron-donating groups form the desired products more quickly



**Table 1**  
Photocatalytic oxidation of benzylamine under visible light irradiation.<sup>a</sup>

Entry	Catalyst	Reaction condition Variations	Light	Time (h)	Conversion <sup>b</sup> (%)
1	BTT-Bpy-COF		On	3	99.9
2 <sup>c</sup>	BTT-Bpy-COF		Off	3	-
3 <sup>d</sup>	BTT-Bpy-COF	no O <sub>2</sub>	On	3	33.3
4	BTT-Bpy-COF	no photocatalyst	On	3	-
5 <sup>e</sup>	BTT-Bpy-COF	L-histidine	On	3	47.9
6 <sup>f</sup>	BTT-Bpy-COF	IPA	On	3	91
7 <sup>g</sup>	BTT-Bpy-COF	p-benzoquinone	On	3	13.4
8 <sup>h</sup>	BTT-Bpy-COF	AgNO <sub>3</sub>	On	3	32
9 <sup>i</sup>	BTT-Bpy-COF	KI	On	3	8.7
10	BTT-BPh-COF		On	3	30
11	BTT-MPh-COF		On	3	42
12	Bp-Bpy-COF		On	3	68
13	Bp-BPh-COF		On	3	-
14	Bp-MPh-COF		On	3	-

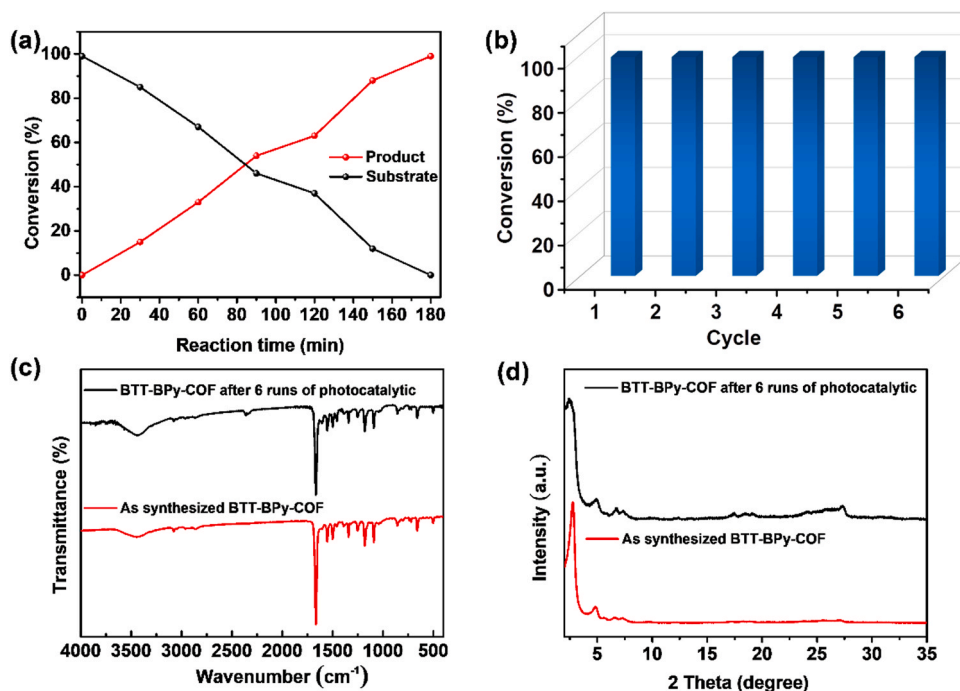
<sup>a</sup> **Reaction condition:** benzylamine (0.5 mmol), photocatalysts (10 mg), 3 mL CH<sub>3</sub>CN, 1 atm O<sub>2</sub>, and 5 W\*4 465 nm LED light source. <sup>b</sup> The conversion was decided by <sup>1</sup>H NMR, GC and GC-MS. <sup>c</sup> In the dark condition. <sup>d</sup> In the air condition. <sup>e</sup> L-histidine was utilized as <sup>1</sup>O<sub>2</sub> radical scavenger. <sup>f</sup> IPA (isopropanol) was utilized as <sup>•</sup>OH radical scavenger. <sup>g</sup> p-benzoquinone was utilized as O<sub>2</sub> radical scavenger. <sup>h</sup> AgNO<sub>3</sub> was utilized as electron scavenger. <sup>i</sup> KI was utilized as hole scavenger.

compared to amines with electron-withdrawing substituted groups (Tables 2, 2a, 2d to 2g, m; b, e to h, k; c, f to i, l). Moreover, when halogen groups are introduced to the reaction, the yield is affected by electronic effects, following the order of -F > -Cl > -Br (Table 2h to k and i to l). Apart from electronic effects, steric effects also play a vital role. For instance, *p*-methylbenzylamine exhibits high conversion compared to other regioisomers, which follow the order *para* > *meta* > *ortho* (Table 2, 2a to 2c; d–f; and g to l). Additionally, heterocyclic amine-like 2-thiophenemethanamine and 2-pyridinemethanamine achieve high conversions of the desired products (Table 2, 2n to o). Overall, substrates with various functional groups can be converted to the corresponding desired

products in a relatively short time. These results further demonstrate the effectiveness of the designed BTT-BPy-COF photocatalyst, and the great tolerance of this catalyst is attributed to its strong light-harvesting capacity resulting from its  $\pi$ -conjugated framework. Cross-coupling reactions were also performed to explore the reaction between benzylamine with different functional groups. As shown in Figures S23–25, cross-coupling can also be performed.

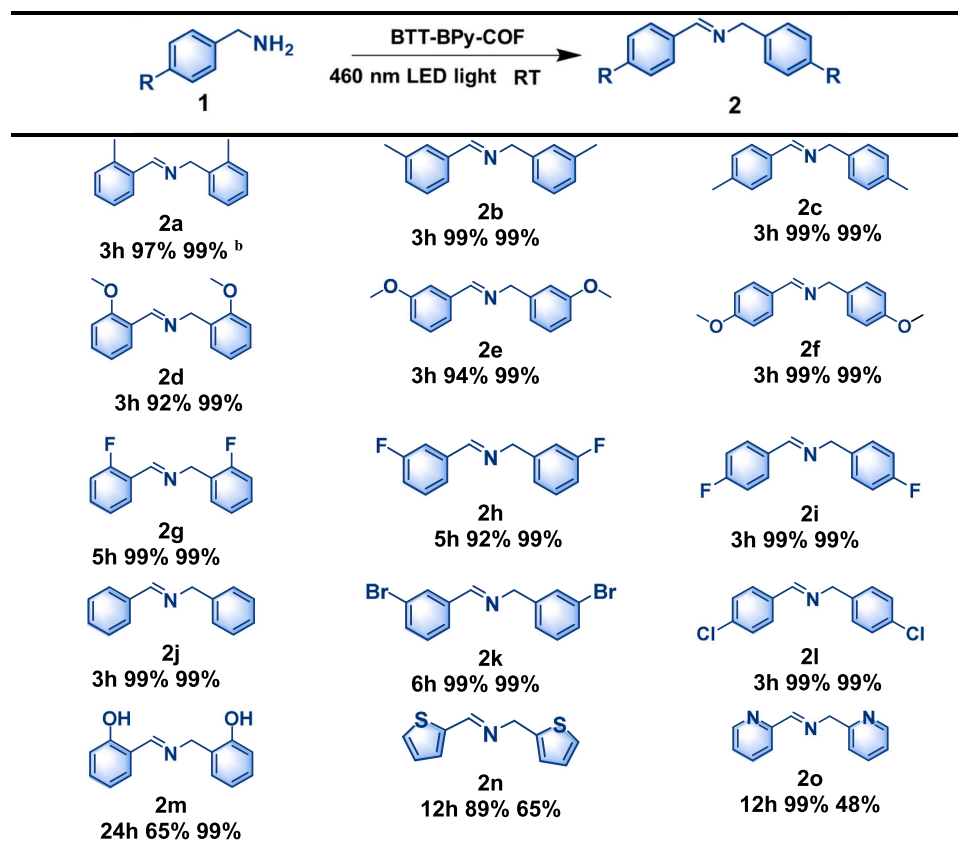
Considering the predominant activity in primary amines, various secondary amines were also introduced to evaluate the performance of BTT-BPy-COF. As depicted in Table 3, every tested secondary amine compound shows high conversion to the desired imine with relatively high selectivity. Considering the existence of larger steric hindrances, secondary amines require more time to complete the reaction. As a typical secondary amine, dibenzylamine can be transformed to N-benzylidenebenzylamine with 90% conversion in 3 h (Table 3, 4a), while 99% of the -OCH<sub>3</sub> substituted dibenzyl amine can be converted within the same time, indicating the influence of electronic effects (Table 3, 4b). This conclusion also applies to N-methylbenzylamine (Table 3, 4c–d). N-isopropyl and N-tert-butyl benzylamine can achieve high conversions, but the activation of  $\alpha$ -hydrogen leads to relatively low selectivity (Table 3, e and f) [61]. Moreover, heterocyclic amine-like indoline and quinoline substrates can be converted to the desired products (Table 3, 4g–k). In addition to exhibiting excellent photocatalytic activity, BTT-BPy-COF can be easily separated by centrifugation, collected, dried at 80 °C, and reused for the next round of the photocatalytic cycle. As shown in Fig. 7b, the conversion and selectivity of benzylamine can be maintained at 99% after six cycles, indicating that BTT-BPy-COF has good photocatalytic stability. The PXRD patterns and FT-IR spectra of this photocatalyst before and after the reaction (Fig. 7c and d) suggest that the chemical structure and characteristic functional groups of BTT-BPy-COF only negligibly decay after reuse. Overall, these results demonstrate the excellent photochemical durability and stability of BTT-BPy-COF.

BTT-BPy-COF was studied using various photoelectrochemical characterization methods to reveal the efficiency of charge separation efficiency and possible mechanism explaining the elevated performance



**Fig. 7.** (a) The conversion vs time plot in the photocatalytic reaction of benzylamine coupling reaction. (b) The recycling experiments of BTT-BPy-COF for photocatalytic reaction of benzylamine coupling reaction. (c) FT-IR patterns of as-synthesized BTT-BPy-COF after 6 runs of photocatalysts. (d) PXRD spectra of as-synthesized BTT-BPy-COF after 6 runs of photocatalysts.



**Table 2**The benzylamine coupling of primary amines to imines by BTT-BPy-COF under visible light irradiation. <sup>a</sup>.

<sup>a</sup> Reaction condition: benzylamine (0.5 mmol), photocatalysts (10 mg), 3 mL CH<sub>3</sub>CN, 1 atm O<sub>2</sub>, and 5 W\*4 465 nm LED light source. <sup>b</sup>The conversion was decided by <sup>1</sup>H NMR, GC and GC-MS.

of this photocatalyst (Fig. 8) [56,61–65]. Under blue LED irradiation, photoexcited electrons (e<sup>-</sup>) move from the HOMO to the LUMO of BTT-BPy-COF, reducing O<sub>2</sub> to <sup>1</sup>O<sub>2</sub> and O<sub>2</sub><sup>-</sup>. This generates holes (h<sup>+</sup>) at the HOMO. Benzylamine is excited by the h<sup>+</sup>, generating the corresponding benzylamine radical cation, which further combines with the above oxygen species to generate benzaldehyde. Finally, the desired product *N*-benzylbenzaldehyde is generated by the condensation of benzaldehyde and benzylamine. By regulating bipyridine-N sites and different linkers, the recombination of photogenerated excitons is reduced while exciton dissociation is encouraged. Thus, BTT-BPy-COF exhibits superior charge transfer and separation properties, which contributes to its excellent performance in the photocatalytic benzylamine coupling reaction. The calculated E<sub>b</sub> values of BTT-BPh-COF and BTT-MPh-COF are 4.37 eV and 4.23 eV, respectively. After introducing bipyridine-N and modulating the linker length, the optimal BTT-BPy-COF has an E<sub>b</sub> value of 3.71 eV, which is much smaller than that of the other two COFs. A lower exciton binding energy facilitates the easier dissociation of excitons into free carriers [31]. This phenomenon enhances the efficiency of the photocatalytic reaction after directional regulation of COFs linkers. The results reported herein also demonstrate that the E<sub>b</sub> values of COFs should be optimized to achieve enhanced photocatalytic performance.

#### 4. Conclusion

In summary, imine-based COFs were designed using aldehyde monomers (BTT and Bp) and three distinct amine units (BPy, BPh, and MPh). The prepared COFs display notably different exciton binding

energies, as evaluated by theoretical calculations, implying that they exhibit significantly different charge separation performance and photocatalytic activity. The photocatalytic performance of the COFs was evaluated by performing the benzylamine coupling reaction, and their activity is in accordance with the theoretical calculations of the excitonic effect. The prepared BTT-BPy-COF photocatalyst, which has the lowest E<sub>b</sub> value, exhibits the highest performance as well as excellent recyclability toward the benzylamine coupling reaction. The pyridine-N of dipyrindine diamine in BTT-BPy-COF also improves the photocatalytic activity. This study realizes the rational design of high-efficiency COF-based photocatalysts by modulating the exciton binding energy and adjusting the monomer linkers, offering a useful strategy for optimizing photocatalytic performance.

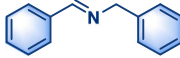
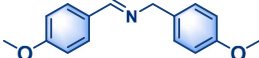
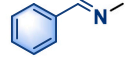
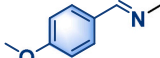
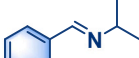
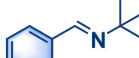

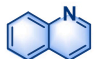

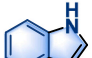
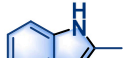
#### Supporting information description

Supporting Information is available and includes the characterization of the catalysts and supports (Figures S1–S18, S26–31, and Table S1–S3), NMR and ESI characterization (Figures S23–S25) of the products, and the theoretical calculation models (Figures S1, S5 and S19–S22, Table S4–S6).

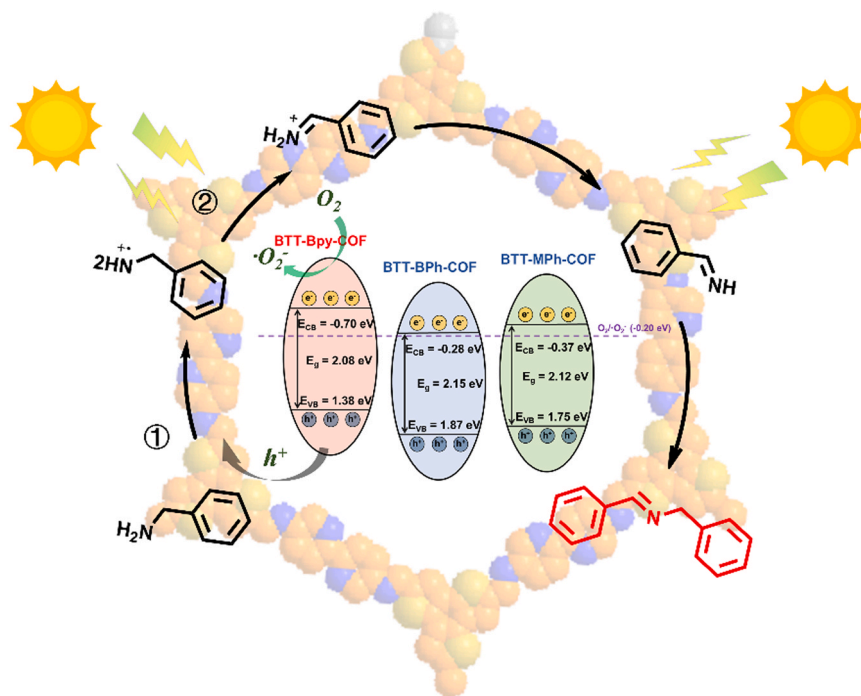
#### CRedit authorship contribution statement

**Jiantai Ma:** Supervision, Resources, Project administration. **Zhengping Dong:** Project administration, Investigation, Supervision, Writing – review & editing. **Liang Li:** Resources, Methodology, Investigation. **Jian Fang:** Resources, Methodology, Investigation. **Ganping**

**Table 3**The benzylamine coupling of secondary amines to imines by BTT-BPy-COF under visible light irradiation. <sup>a</sup>.

$  \begin{array}{c}  \text{R} \\    \\  \text{C}_6\text{H}_4\text{CH}_2\text{NHR}_1 \\  \text{3}  \end{array}  \xrightarrow[\text{460 nm LED light RT}]{\text{BTT-BPy-COF}}  \begin{array}{c}  \text{R} \\    \\  \text{C}_6\text{H}_4\text{CH=N-R}_1 \\  \text{4}  \end{array}  $		
 <b>4a</b> 3h 90% 99% <sup>b</sup>	 <b>4b</b> 4h 99% 99%	 <b>4c</b> 4h 99% 54%
 <b>4d</b> 4h 99% 99%	 <b>4e</b> 8h 99% 54%	 <b>4f</b> 4h 99% 99%
 <b>4g</b> 12h 99% 53%	 <b>4h</b> 12h 83% 99%	 <b>4i</b> 12h 83% 99%
 <b>4j</b> 12h 89% 99%	 <b>4k</b> 12h 89% 99%	

<sup>a</sup> **Reaction condition:** benzylamine (0.5 mmol), photocatalysts (10 mg), 3 mL CH<sub>3</sub>CN, 1 atm O<sub>2</sub>, and 5 W \* 4 465 nm LED light source. <sup>b</sup> The conversion was decided by <sup>1</sup>H NMR, GC and GC-MS.

**Fig. 8.** The possible reaction mechanism of benzylamine coupling.

**Wang:** Writing – original draft, Software, Resources, Methodology.  
**Hongyan Guo:** Resources, Investigation, Formal analysis, Data curation.  
**Jinfang Kou:** Writing – original draft, Investigation, Formal analysis, Conceptualization.

**Declaration of Competing Interest**

The authors declare that they have no known competing financial

interests or personal relationships that could have appeared to influence the work reported in this paper.

**Data Availability**

Data will be made available on request.

## Acknowledgements

The research was supported by the National Natural Science Foundation of China (Nos. 22172067 and U21B2091).

## Appendix A. Supporting information

Supplementary data associated with this article can be found in the online version at doi:10.1016/j.apcatb.2024.124020.

## References

- [1] Y. He, Y. Zhao, X. Wang, Z. Liu, Y. Yu, L. Li, Multiple heteroatom-hydrogen bonds bridging electron transport in covalent organic framework-based supramolecular system for photoreduction of CO<sub>2</sub>, *Angew. Chem. Int. Ed.* 62 (2023) e202307160.
- [2] I. Sullivan, A. Goryachev, I.A. Digdaya, X. Li, H.A. Atwater, D.A. Vermaas, C. Xiang, Coupling electrochemical CO<sub>2</sub> conversion with CO<sub>2</sub> capture, *Nat. Catal.* 4 (2021) 952–958.
- [3] M. Lu, S.-B. Zhang, M.-Y. Yang, Y.-F. Liu, J.-P. Liao, P. Huang, M. Zhang, S.-L. Li, Z.-M. Su, Y.-Q. Lan, Dual photosensitizer coupled three-dimensional metal-covalent organic frameworks for efficient photocatalytic reactions, *Angew. Chem. Int. Ed.* 62 (2023) e202307632.
- [4] S. Bi, P. Thiruvengadam, S. Wei, W. Zhang, F. Zhang, L. Gao, J. Xu, D. Wu, J.-S. Chen, F. Zhang, Vinylene-bridged two-dimensional covalent organic frameworks via Knoevenagel condensation of tricyanomesitylene, *J. Am. Chem. Soc.* 142 (2020) 11893–11900.
- [5] Q. Wang, K. Domen, Particulate photocatalysts for light-driven water splitting: mechanisms, challenges, and design strategies, *Chem. Rev.* 120 (2020) 919–985.
- [6] A. Kudo, Y. Miseki, Heterogeneous photocatalyst materials for water splitting, *Chem. Soc. Rev.* 38 (2009) 253–278.
- [7] J. Ran, J. Zhang, J. Yu, M. Jaroniec, S.Z. Qiao, Earth-abundant cocatalysts for semiconductor-based photocatalytic water splitting, *Chem. Soc. Rev.* 43 (2014) 7787–7812.
- [8] A. Fujishima, K. Honda, Electrochemical photolysis of water at a semiconductor electrode, *Nature* 238 (1972) 37–38.
- [9] F.E. Osterloh, Inorganic nanostructures for photoelectrochemical and photocatalytic water splitting, *Chem. Soc. Rev.* 42 (2013) 2294–2320.
- [10] H. Song, S. Luo, H. Huang, B. Deng, J. Ye, Solar-driven hydrogen production: recent advances, challenges, and future perspectives, *ACS Energy Lett.* 7 (2022) 1043–1065.
- [11] T. Banerjee, F. Podjaski, J. Kröger, B.P. Biswal, B.V. Lotsch, Polymer photocatalysts for solar-to-chemical energy conversion, *Nat. Rev. Mater.* 6 (2021) 168–190.
- [12] L. Lin, Z. Yu, X. Wang, Crystalline carbon nitride semiconductors for photocatalytic water splitting, *Angew. Chem. Int. Ed.* 58 (2019) 6164–6175.
- [13] H. Wang, S. Jin, X. Zhang, Y. Xie, Excitonic effects in polymeric photocatalysts, *Angew. Chem. Int. Ed.* 59 (2020) 22828–22839.
- [14] X. Wang, L. Chen, S.Y. Chong, M.A. Little, Y. Wu, W.-H. Zhu, R. Clowes, Y. Yan, M. A. Zwiijnenburg, R.S. Sprick, A.I. Cooper, Sulfone-containing covalent organic frameworks for photocatalytic hydrogen evolution from water, *Nat. Chem.* 10 (2018) 1180–1189.
- [15] M.G. Schwab, M. Hamburger, X. Feng, J. Shu, H.W. Spiess, X. Wang, M. Antonietti, K. Müllen, Photocatalytic hydrogen evolution through fully conjugated poly (azomethine) networks, *Chem. Commun.* 46 (2010) 8932–8934.
- [16] R.S. Sprick, J.-X. Jiang, B. Bonillo, S. Ren, T. Ratvijitvech, P. Guiglion, M. A. Zwiijnenburg, D.J. Adams, A.I. Cooper, Tunable organic photocatalysts for visible-light-driven hydrogen evolution, *J. Am. Chem. Soc.* 137 (2015) 3265–3270.
- [17] C. Yang, B.C. Ma, L. Zhang, S. Lin, S. Ghasimi, K. Landfester, K.A.I. Zhang, X. Wang, Molecular engineering of conjugated polybenzothiadiazoles for enhanced hydrogen production by photosynthesis, *Angew. Chem. Int. Ed.* 55 (2016) 9202–9206.
- [18] K. Wang, L.-M. Yang, X. Wang, L. Guo, G. Cheng, C. Zhang, S. Jin, B. Tan, A. Cooper, Covalent triazine frameworks via a low-temperature polycondensation approach, *Angew. Chem. Int. Ed.* 56 (2017) 14149–14153.
- [19] G. Zhang, G. Li, Z.-A. Lan, L. Lin, A. Savateev, T. Heil, S. Zafeirotas, X. Wang, M. Antonietti, Optimizing optical absorption, exciton dissociation, and charge transfer of a polymeric carbon nitride with ultrahigh solar hydrogen production activity, *Angew. Chem. Int. Ed.* 56 (2017) 13445–13449.
- [20] V. Coropceanu, J. Cornil, D.A. da Silva Filho, Y. Olivier, R. Silbey, J.-L. Brédas, Charge transport in organic semiconductors, *Chem. Rev.* 107 (2007) 926–952.
- [21] Y. Cao, I.D. Parker, G. Yu, C. Zhang, A.J. Heeger, Improved quantum efficiency for electroluminescence in semiconducting polymers, *Nature* 397 (1999) 414–417.
- [22] J. Kosco, M. Bidwell, H. Cha, T. Martin, C.T. Howells, M. Sachs, D.H. Anjum, S. Gonzalez Lopez, L. Zou, A. Wadsworth, W. Zhang, L. Zhang, J. Tellam, R. Sougrat, F. Laquai, D.M. DeLongchamp, J.R. Durrant, I. McCulloch, Enhanced photocatalytic hydrogen evolution from organic semiconductor heterojunction nanoparticles, *Nat. Mater.* 19 (2020) 559–565.
- [23] Y. Wang, A. Vogel, M. Sachs, R.S. Sprick, L. Wilbraham, S.J.A. Moniz, R. Godin, M. A. Zwiijnenburg, J.R. Durrant, A.I. Cooper, J. Tang, Current understanding and challenges of solar-driven hydrogen generation using polymeric photocatalysts, *Nat. Energy* 4 (2019) 746–760.
- [24] C.S. Diercks, O.M. Yaghi, The atom, the molecule, and the covalent organic framework, *Science* 355 (2017) eaal1585.
- [25] C. Kang, Z. Zhang, A.K. Usadi, D.C. Calabro, L.S. Baugh, K. Yu, Y. Wang, D. Zhao, Aggregated structures of two-dimensional covalent organic frameworks, *J. Am. Chem. Soc.* 144 (2022) 3192–3199.
- [26] H.S. Sasmal, A. Kumar Mahato, P. Majumder, R. Banerjee, Landscaping covalent organic framework nanomorphologies, *J. Am. Chem. Soc.* 144 (2022) 11482–11498.
- [27] B. Han, X. Ding, B. Yu, H. Wu, W. Zhou, W. Liu, C. Wei, B. Chen, D. Qi, H. Wang, K. Wang, Y. Chen, B. Chen, J. Jiang, Two-dimensional covalent organic frameworks with cobalt(II)-phthalocyanine sites for efficient electrocatalytic carbon dioxide reduction, *J. Am. Chem. Soc.* 143 (2021) 7104–7113.
- [28] C. Han, S. Xiang, S. Jin, C. Zhang, J.-X. Jiang, Rational design of conjugated microporous polymer photocatalysts with definite D–π–A structures for ultrahigh photocatalytic hydrogen evolution activity under natural sunlight, *ACS Catal.* 13 (2023) 204–212.
- [29] W. Zhao, D. Zhai, C. Liu, D. Zheng, H. Wu, L. Sun, Z. Li, T. Yu, W. Zhou, X. Fang, S. Zhai, K. Han, Z. He, W.-q. Deng, Unlocked intramolecular charge transfer for enhanced CO<sub>2</sub> photoreduction enabled by an imidazolium-based ionic conjugated microporous polymer, *Appl. Catal. B Environ.* 300 (2022) 120719.
- [30] Y. Qian, D. Li, Y. Han, H.-L. Jiang, Photocatalytic molecular oxygen activation by regulating excitonic effects in covalent organic frameworks, *J. Am. Chem. Soc.* 142 (2020) 20763–20771.
- [31] Y. Qian, Y. Han, X. Zhang, G. Yang, G. Zhang, H.-L. Jiang, Computation-based regulation of excitonic effects in donor-acceptor covalent organic frameworks for enhanced photocatalysis, *Nat. Commun.* 14 (2023) 3083.
- [32] K. Xiong, Y. Wang, F. Zhang, X. Li, X. Lang, Linker length-dependent photocatalytic activity of β-ketoenamine covalent organic frameworks, *Appl. Catal. B Environ.* 322 (2023) 122135.
- [33] H.-W. Liang, X. Zhuang, S. Brüller, X. Feng, K. Müllen, Hierarchically porous carbons with optimized nitrogen doping as highly active electrocatalysts for oxygen reduction, *Nat. Commun.* 5 (2014) 4973.
- [34] R. Liu, D. Wu, X. Feng, K. Müllen, Nitrogen-doped ordered mesoporous graphitic arrays with high electrocatalytic activity for oxygen reduction, *Angew. Chem. Int. Ed.* 49 (2010) 2565–2569.
- [35] W. Ding, Z. Wei, S. Chen, X. Qi, T. Yang, J. Hu, D. Wang, L.-J. Wan, S.F. Alvi, L. Li, Space-confinement-induced synthesis of pyridinic- and pyrrolic-nitrogen-doped graphene for the catalysis of oxygen reduction, *Angew. Chem. Int. Ed.* 52 (2013) 11755–11759.
- [36] D. Guo, R. Shibuya, A. Akiba, S. Saji, T. Kondo, J. Nakamura, Active sites of nitrogen-doped carbon materials for oxygen reduction reaction clarified using model catalysts, *Science* 351 (2016) 361–365.
- [37] F. Chu, G. Hai, D. Zhao, S. Liu, Y. Hu, G. Zhao, B. Peng, G. Wang, X. Huang, Regulating keto–enol tautomerism of β-ketoenamine covalent–organic frameworks for photocatalytic oxidative coupling of amines, *ACS Catal.* 13 (2023) 13167–13180.
- [38] J.-D. Chai, M. Head-Gordon, Long-range corrected hybrid density functionals with damped atom–atom dispersion corrections, *Phys. Chem. Chem. Phys.* 10 (2008) 6615–6620.
- [39] P.K. Nayak, N. Periasamy, Calculation of electron affinity, ionization potential, transport gap, optical band gap and exciton binding energy of organic solids using ‘solvation’ model and DFT, *Org. Electron* 10 (2009) 1396–1400.
- [40] T. Lu, F. Chen, Multiwfn: a multifunctional wavefunction analyzer, *J. Comput. Chem.* 33 (2012) 580–592.
- [41] Z. Liu, T. Lu, Q. Chen, An sp-hybridized all-carboatomic ring, cyclo[18]carbon: electronic structure, electronic spectrum, and optical nonlinearity, *Carbon* 165 (2020) 461–467.
- [42] G. Kresse, J. Furthmüller, Efficient iterative schemes for ab initio total-energy calculations using a plane-wave basis set, *Phys. Rev. B* 54 (1996) 11169–11186.
- [43] J.P. Perdew, K. Burke, M. Ernzerhof, Generalized gradient approximation made simple, *Phys. Rev. Lett.* 77 (1996) 3865–3868.
- [44] J. Heyd, G.E. Scuseria, Efficient hybrid density functional calculations in solids: assessment of the Heyd–Scuseria–Ernzerhof screened Coulomb hybrid functional, *J. Chem. Phys.* 121 (2004) 1187–1192.
- [45] S. Yang, W. Hu, X. Zhang, P. He, B. Pattengale, C. Liu, M. Cendejas, I. Hermans, X. Zhang, J. Zhang, J. Huang, 2D covalent organic frameworks as intrinsic photocatalysts for visible light-driven CO<sub>2</sub> reduction, *J. Am. Chem. Soc.* 140 (2018) 14614–14618.
- [46] Y.-N. Gong, W. Zhong, Y. Li, Y. Qiu, L. Zheng, J. Jiang, H.-L. Jiang, Regulating photocatalysis by spin-state manipulation of cobalt in covalent organic frameworks, *J. Am. Chem. Soc.* 142 (2020) 16723–16731.
- [47] C. Feriante, A.M. Evans, S. Jhulki, I. Castano, M.J. Strauss, S. Barlow, W.R. Dichtel, S.R. Marder, New mechanistic insights into the formation of imine-linked two-dimensional covalent organic frameworks, *J. Am. Chem. Soc.* 142 (2020) 18637–18644.
- [48] L. Guo, Y. Niu, H. Xu, Q. Li, S. Razzaque, Q. Huang, S. Jin, B. Tan, Engineering heteroatoms with atomic precision in donor–acceptor covalent triazine frameworks to boost photocatalytic hydrogen production, *J. Mater. Chem. A* 6 (2018) 19775–19781.
- [49] S. Kraner, G. Prampolini, G. Cuniberti, Exciton binding energy in molecular triads, *J. Phys. Chem. C* 121 (2017) 17088–17095.
- [50] S. Kraner, R. Scholz, F. Plasser, C. Koerner, K. Leo, Exciton size and binding energy limitations in one-dimensional organic materials, *J. Chem. Phys.* 143 (2015) 244905.
- [51] Z.-A. Lan, M. Wu, Z. Fang, X. Chi, X. Chen, Y. Zhang, X. Wang, A fully coplanar donor–acceptor polymeric semiconductor with promoted charge separation kinetics for photochemistry, *Angew. Chem. Int. Ed.* 60 (2021) 16355–16359.

- [52] J. Kou, J. Fang, J. Li, H. Zhao, M. Gao, G. Zeng, W. David Wang, F. Zhang, J. Ma, Z. Dong, Electron-rich platinum single sites anchored on sulfur-doped covalent organic frameworks for boosting anti-Markovnikov hydrosilylation of alkenes, *Chem. Eng. J.* 463 (2023) 142255.
- [53] S. Barman, A. Singh, F.A. Rahimi, T.K. Maji, Metal-free catalysis: a redox-active donor-acceptor conjugated microporous polymer for selective visible-light-driven CO<sub>2</sub> reduction to CH<sub>4</sub>, *J. Am. Chem. Soc.* 143 (2021) 16284–16292.
- [54] M. Bhadra, S. Kandambeth, M.K. Sahoo, M. Addicoat, E. Balaraman, R. Banerjee, Triazine functionalized porous covalent organic framework for photo-organocatalytic E–Z isomerization of olefins, *J. Am. Chem. Soc.* 141 (2019) 6152–6156.
- [55] B. Jürgens, E. Irran, J. Senker, P. Kroll, H. Müller, W. Schnick, Melem (2,5,8-Triamino-tri-s-triazine), an important intermediate during condensation of melamine rings to graphitic carbon nitride: synthesis, structure determination by X-ray powder diffractometry, solid-state NMR, and theoretical studies, *J. Am. Chem. Soc.* 125 (2003) 10288–10300.
- [56] X. Li, S. Yang, F. Zhang, L. Zheng, X. Lang, Facile synthesis of 2D covalent organic frameworks for cooperative photocatalysis with TEMPO: the selective aerobic oxidation of benzyl amines, *Appl. Catal. B Environ.* 303 (2022) 120846.
- [57] Q. Song, W. David Wang, K. Lu, F. Li, B. Wang, L. Sun, J. Ma, H. Zhu, B. Li, Z. Dong, Three-dimensional hydrophobic porous organic polymers confined Pd nanoclusters for phase-transfer catalytic hydrogenation of nitroarenes in water, *Chem. Eng. J.* 415 (2021) 128856.
- [58] H. Wei, J. Ning, X. Cao, X. Li, L. Hao, Benzotrithiophene-based covalent organic frameworks: construction and structure transformation under ionothermal condition, *J. Am. Chem. Soc.* 140 (2018) 11618–11622.
- [59] X. Ma, G. Wang, L. Qin, J. Liu, B. Li, Y. Hu, H. Cheng, Z-scheme g-C<sub>3</sub>N<sub>4</sub>-AQ-MoO<sub>3</sub> photocatalyst with unique electron transfer channel and large reduction area for enhanced sunlight photocatalytic hydrogen production, *Appl. Catal. B Environ.* 288 (2021) 120025.
- [60] W. Liu, Y. Wang, H. Huang, J. Wang, G. He, J. Feng, T. Yu, Z. Li, Z. Zou, Spatial decoupling of redox chemistry for efficient and highly selective amine photoconversion to imines, *J. Am. Chem. Soc.* 145 (2023) 7181–7189.
- [61] S. Li, L. Li, Y. Li, L. Dai, C. Liu, Y. Liu, J. Li, J. Lv, P. Li, B. Wang, Fully conjugated donor-acceptor covalent organic frameworks for photocatalytic oxidative amine coupling and thioamide cyclization, *ACS Catal.* 10 (2020) 8717–8726.
- [62] K. Wu, X.-Y. Liu, P.-W. Cheng, Y.-L. Huang, J. Zheng, M. Xie, W. Lu, D. Li, Linker engineering for reactive oxygen species generation efficiency in ultra-stable nickel-based metal-organic frameworks, *J. Am. Chem. Soc.* 145 (2023) 18931–18938.
- [63] Y. Nosaka, A.Y. Nosaka, Generation and detection of reactive oxygen species in photocatalysis, *Chem. Rev.* 117 (2017) 11302–11336.
- [64] F. Huang, X. Dong, Y. Wang, X. Lang, Narrowing the bandgaps of thiazolo[5,4-d]thiazole-bridged conjugated microporous polymers to capture green light for selective oxidation of amines, *Appl. Catal. B Environ.* 330 (2023) 122585.
- [65] Z. Wu, X. Huang, X. Li, G. Hai, B. Li, G. Wang, Covalent-organic frameworks with keto-enol tautomerism for efficient photocatalytic oxidative coupling of amines to imines under visible light, *Sci. China Chem.* 64 (2021) 2169–2179.